Heparan sulfate assists SARS-CoV-2 in cell entry and can be targeted by approved drugs *in vitro*

Qi Zhang[1], Catherine Z. Chen[2], Manju Swaroop[2], Miao Xu[2], Lihui Wang[1], Juhyung Lee[1], Amy Q. Wang[2], Manisha Pradhan[2], Natalie Hagen[2], Lu Chen[2], Min Shen[2], Zhiji Luo[2], Xin Xu[2], Yue Xu[1], Wenwei Huang[2], Wei Zheng[2], Yihong Ye[1]

[1] Laboratory of Molecular Biology, National Institute of Diabetes and Digestive and Kidney Diseases, National Institutes of Health, Bethesda, MD 20892

[2] National Center for Advancing Translational Sciences, National Institutes of Health, Rockville, MD 20850

Correspondence should be sent to:

Yihong Ye

email: yihongy@mail.nih.gov

Tel: 301-594-0845

Fax: 301-496-0201

Running title: Targeting HS as a COVID-19 therapy

Keywords: SARS-CoV-2; coronavirus; cell entry; COVID-19; endocytosis; drug repurposing screen; heparan sulfate; heparin; actin cytoskeleton; Tilorone; Mitoxantrone; Raloxifene

The cell entry of SARS-CoV-2 has emerged as an attractive drug repurposing target for COVID-19. Here we combine genetics and chemical perturbation to demonstrate that ACE2-mediated entry of SARS-CoV and CoV-2 requires the cell surface heparan sulfate (HS) as an assisting cofactor: ablation of genes involved in HS biosynthesis or incubating cells with a HS mimetic both inhibit Spike-mediated viral entry. We show that heparin/HS binds to Spike directly, facilitates the attachment of viral particles to the cell surface to promote cell entry. We screened approved drugs and identified two classes of inhibitors that act via distinct mechanisms to target this entry pathway. Among the drugs characterized, Mitoxantrone is a potent HS inhibitor, while Sunitinib and BNTX disrupt the actin network to indirectly abrogate HS-assisted viral entry. We further show that drugs of the two classes can be combined to generate a synergized activity against SARS-CoV-2-induced cytopathic effect. Altogether, our study establishes HS as an attachment factor that assists SARS coronavirus cell entry, and reveals drugs capable of targeting this important step in the viral life cycle.

The ongoing pandemic of the coronavirus disease 2019 (COVID-19) has claimed many lives and severely damaged the global economy. This severe acute respiratory syndrome (SARS) is caused by a novel coronavirus SARS-CoV-2 [1, 2], which is closely related to SARS-CoV, the virus underlying the 2003 SARS outbreak [3].

As a positive-sense, single-stranded RNA virus bearing a membrane envelope, coronavirus enters cells when this membrane envelope fuses with host membranes [4]. Viral entry may take place either at the plasma membrane or at the endosomes following receptor-mediated endocytosis [5]. Previous studies showed that SARS-CoV enters cells primarily through ACE2-dependent endocytosis [5-9]. New evidence suggests that SARS-CoV-2 may follow the same entry path [1, 10, 11]. Specifically, limiting the production of phosphatidylinositol 4,5-bisphosphate (PIP2) inhibits the fusion of the SARS-CoV-2 envelop with the endolysosomes and viral entry [12, 13]. Additionally, viral entry-associated membrane fusion requires a priming step mediated by several host proteases including the lysosome-localized Cathepsin B/L and serine proteases of the TMPRSS family [12, 14-18]. Although some TMPRSS proteases may act on the cell surface, the fact that increasing the lysosomal pH in either TMPRSS2 positive Caco-2 or TMPRSS2 negative HEK293 cells both inhibits SARS-CoV-2 cell entry [14] suggests endolysosomes as a major entry site for SARS-CoV-2 at least in certain cell types.

Our previous study on the intercellular transmission of misfolded α-Synuclein (α-Syn) fibrils, a cellular process reminiscent of viral infection, revealed an endocytosis mechanism by which the cell surface heparan sulfate (HS) facilitates receptor-mediated uptake of protein assemblies bearing excess positive charges [19]. HS is a negative charge-enriched linear polysaccharide molecule that is attached to several membrane and extracellular proteins, which are collectively termed as heparan sulfate proteoglycans (HSPG). The cell surface HS can serve

3

as an anchor point to facilitate endocytosis of many cargos [20, 21], which include SARS-CoV-2 related coronaviruses [22-25]. To identify drugs that can diminish the spreading of misfolded α-Syn and the associated Parkinsonism [26], we screen and identify eight FDA-approved drugs that block the HS-dependent endocytosis of preformed α-Syn fibrils (see below). Intriguingly, one of the candidates Tilorone was recently reported as an inhibitor of SARS-CoV-2 infection [27]. This coincidence, together with the recently reported interaction of SARS-CoV-2 Spike with the HS mimetic glycan heparin [28-30] and other evidence in support of a role for HS in the entry of SARS-CoV-2-related coronaviruses [22-25, 31] prompted us to investigate the possibility of targeting HS as a COVID-19 therapeutic strategy.

Results

Heparan sulfate facilitates Spike-dependent viral entry

To study Spike-mediated viral entry, we constructed luciferase-expressing pseudoviral particles (PP) bearing SARS-CoV or SARS-CoV-2 Spike. We infected HEK293T (human embryonic kidney cells) cells or HEK293T cells stably expressing ACE2-GFP with PP. As expected, ACE2-GFP HEK293T cells transduced with SARS-CoV or SARS-CoV-2 PP expressed luciferase significantly higher than non-infected ACE2-GFP cells (Fig. S1A, B) or infected HEK293T cells without ACE2-GFP (Fig. S1C). These results confirm Spike-dependent entry of SARS-CoV and CoV-2 via ACE2.

To test the role of HS in viral entry, we first treated ACE2-GFP HEK293T cells with heparin, a HS mimetic glycan frequently used as a competitive inhibitor for HS ligands (Figure 1A) [32, 33]. Heparin treatment dose-dependently mitigated luciferase expression from both SARS-CoV and CoV-2 PP (Figure 1B, C) with little impact on cell viability (Fig. S1D). Heparin

4

treatment also reduced luciferase expression in SARS-CoV- or CoV-2-transduced human lung epithelial Calu-3 cells (Fig. S1E) and the level of inhibition was more significant than in ACE2-GFP overexpressing cells. Heparin pulldown showed that the purified Spike ectodomain readily bound to heparin-conjugated beads (Figure 1D). As expected, the interaction was sensitive to salt, but a significant amount of Spike remained associated with heparin in a buffer containing 120mM NaCl (Fig. S1F), a condition recapitulating the airway surface salt concentration [34]. These data suggest that heparin acts as a competitive inhibitor for Spike-mediated viral entry and this inhibitory activity could be offset by overexpression of ACE2.

Next, we used small interfering RNA (siRNA) or CRISPR to disrupt genes encoding HSPG biosynthetic enzyme XYLT2 and SLC35B2 [19] (Figure 2A, Fig. S1G-I). *XYLT2* encodes one of the two HS chain initiation enzymes. SLC35B2 is a Golgi-localized transporter for 3'-phosphoadenosine 5'-phosphosulfate (PAPS), which is essential for HS chain sulfation [32]. Knockdown of *XLYT2* by ~80% inhibited SARS-CoV and SARS-CoV-2 PP entry similarly as heparin treatment (Figure 2B). By contrast, CRISPR-mediated inactivation of *SLC35B2* completely abolished HSPG biosynthesis [19] and thus inhibited the entry of SARS-CoV and SARS-CoV-2 more dramatically (Figure 2C). Analyses of GFP fluorescence showed no effect of *SCL35B2* knockout on ACE2-GFP expression (Fig. S1J). Nevertheless, the knockout of *SLC35B2* significantly reduced the binding of SARS-CoV-2 PP to ACE2-GFP cells (Figure 2D, E). Altogether, these results support a model in which the cell surface HS serves as a virus-recruiting factor to promote ACE2-dependent viral entry.

A drug screen identifies inhibitors targeting the HS-dependent cell entry pathway

5

HS is a negatively charged biopolymer, which can recruit ligands bearing positive charges to facilitate their endocytosis [20]. We recently characterized the endocytosis mechanism of α-Syn fibril, which is a HS ligand [19]. We then conducted a quantitative high-throughput (qHTS) screen using α-Syn filamentous inclusions to search for approved drugs that could block HS-dependent endocytosis (Figure 3A). The screen identified 8 drugs that inhibited α-Syn fibril uptake in HEK293T cells (Figure 3B). Additional studies using a panel of endocytosis cargos confirmed that the identified drugs are endocytosis inhibitors with a preference for HS-dependent ligands (Figure 3C). Among the cargos tested, supercharged GFP (GFP+), polycation-coated DNA, and VSVG-pseudotyped lentivirus all enter cells via a *SLC35B2* dependent mechanism [19, 35], whereas Transferrin uses a HS independent but clathrin-dependent endocytosis pathway. The cholera toxin B chain (CTB) reaches the Golgi apparatus via a clathrin-independent mechanism [36]. None of the drugs tested affected the internalization of CTB, but Sunitinib and BNTX appeared to disrupt the perinuclear stacking of the Golgi system (Fig. S2A, B). These drugs also had little impact on Transferrin endocytosis (Fig. S2C), but they could reduce the uptake of HS-dependent cargos to various levels with Mitoxantrone being the most potent one: at $5\,\mu$M, it almost completely blocked the endocytosis of all HS-dependent cargos tested (Figure 3C, Fig. S2D-F).

Biochemical binding coupled to mass spectrometry analyses showed that these drugs could be categorized into two classes depending on whether they bound to heparin. While Exifone, K114, Tilorone, BNTX, and Sunitinib showed no affinity to heparin, Mitoxantrone, Raloxifene, and Piceatannol in solution could be effectively depleted by heparin beads (Figure 3D), suggesting that these drugs amy target the cell surface HS directly to inhibit cargo uptake.

Among the drugs identified, Tilorone was previously established as a pan-antiviral agent [37] that also inhibits SARS-CoV-2 infection *in vitro* [27]. This coincidence, together with the

convergence of SARS-CoV and CoV-2 entry and α-Syn endocytosis at the HS glycans raise the possibility that inhibitors of HS-dependent endocytosis might also block SARS-CoV and CoV-2 entry. Indeed, with the exception of Exifone and K114, other drugs could all mitigate Spike-mediated viral entry in ACE2-GFP cells (Fig. S3A and see below). Exifone and K114 were excluded from further study.

The actin network is required for Spike-mediated viral entry

We chose representative drugs of the two classes for further characterization. For those that did not bind heparin, we characterized BNTX and Sunitinib because their effect on Golgi morphology suggested a potential shared mechanism. BNTX is an opioid receptor antagonist for opioid or alcohol use disorders, while Sunitinib has been used as a receptor tyrosine kinase inhibitor for cancer therapy [38]. In HEK293 ACE2-GFP cells treated with SARS-CoV or SARS-CoV-2 PP, these drugs inhibited viral entry with respective IC$_{50}$ of ~30μM and 10μM for Sunitinib, 9μM and 10μM for BNTX (Figure 4A, B). In Vero E6 cells treated with wild-type SARS-CoV-2, BNTX at 2 μM rescued the virus-induced CPE by ~70%, whereas 10μM Sunitinib rescued the CPE only by ~30% (Figure 4C, Fig. S3B).

Because HS-assisted endocytosis often requires the actin cytoskeleton [19], we determined whether these drugs affect the actin cytoskeleton network using U2OS cells stably expressing Tractin-EGFP, an actin filament label [39]. Confocal microscopy showed that actin monomers polymerize near peripheral membranes in untreated cells, forming a microfilament network with parallel actin filaments (Fig. S3C). Additionally, a meshwork of actin is associated with the cell cortex, while thick actin bundles named stress fibers are often found near basal membranes. In cells exposed to Sunitinib, the actin microfilaments were frequently replaced by short disoriented

7

actin segments. Many cells also contained an increased number of filopodia. By contrast, cells treated with BNTX had significantly reduced number of actin filaments, with many cells containing actin-positive aggregates (Fig. S3C, top panels). These phenotypes were further confirmed by TIRF microscopy in Sunitinib- or BNT-treated cells but were not observed in cells treated with other drugs (Fig. S3C, D).

To further elucidate the actions of Sunitinib and BNTX, we used live-cell imaging to monitor the acute changes in actin dynamics in drug-treated cells. Shortly after Sunitinib treatment, we observed extensive de novo actin filament formation (Figure 4D, E, Supplementary movies 2 vs. 1). Actin polymerization was also detected in the cell periphery where it drove filopodium formation (Figure 4D) but was not seen near basal membranes where stress fibers were located (Supplementary movie 4 vs. 3). Unlike Sunitinib, BNTX treatment resulted in rapid shrinking of actin microfilaments and the loss of membrane ruffling in the peripheral cortex (Figure 4F, G, Supplementary movies 6 vs. 5). These data suggest that Sunitinib promotes actin assembly to form disoriented filaments, whereas BNTX disrupts the cortex actin meshwork either by promoting actin disassembly or inhibiting actin assembly. The fact that two structurally unrelated actin inhibitors both block SARS-CoV and CoV-2 entry strongly suggests that the entry of these viruses may require the actin cytoskeleton. Accordingly, SARS-CoV-2 PP entry was also inhibited by Latrunculin A, a well-established actin inhibitor (Figure 4H). These findings, together with the fact that Sunitinib was previously identified as an entry inhibitor for Ebola virus [40] highlight an important role played by actin in the entry of these RNA envelop viruses.

Mitoxantrone inhibits viral entry by targeting HS

Among drugs bound to heparin, Mitoxantrone had a higher affinity. Mitoxantrone was previously reported as a DNA intercalator, which also inhibits type II DNA topoisomerase [41, 42]. Accordingly, Mitoxantrone is currently approved for treatment of acute non-lymphocytic leukemia, prostate cancer, and multiple sclerosis. In PP-treated ACE2-GFP HEK293 cells, Mitoxantrone strongly inhibited viral entry with IC_{50} >100-fold lower than that of cytotoxicity, suggesting an excellent anti-viral therapeutic window (Figure 5A).

Because Mitoxantrone has absorbance peaks at 620 nm and 685 nm (Fig. S4A). we used this spectral property to trace its localization in drug-treated cells, which hinted at its cellular target. To this end, we performed subcellular fractionation using Mitoxantrone-treated cells to obtain the nucleus (1,000g pellet), mitochondria-enriched heavy membrane (7,000g pellet), light membrane (100,000g pellet), and cytosol (100,000g supernatant) fractions (Figure 5B top panel). Although blue color was seen in every pellet fraction, Mitoxantrone in the nucleus and heavy membrane fractions was resistant to extraction by a buffer containing the non-ionic detergent NP40 or 1% SDS, probably due to tight association with DNA. By contrast, Mitoxantrone in the light membranes (containing the plasma membrane and endoplasmic reticulum as demonstrated by immunoblotting, middle panel) could be readily released by an NP40-containing buffer and detected by a spectrometer (Figure 5B). No Mitoxantrone was detected in the cytosol fraction. Thus, in addition to DNA, Mitoxantrone also binds to cell membranes.

Several lines of evidence suggest that Mitoxantrone targets the cell surface HS directly. First, the amount of P100-associated Mitoxantrone from *SLC35B2* deficient cells (lacking HS) was significantly lower than that of wild-type cells, which could be rescued by re-expression of SLC35B2 (Figure 5C). Additionally, as mentioned above, Mitoxantrone readily bound to heparin, a glycan structurally related to HS (Figure 3F, Fig. S4B). Because the interaction of heparin with

9

Mitoxantrone lowered its absorption spectrum in solution (Fig. S4C), we used this property to further determine the interaction of Mitoxantrone with other related glycans. As expected, HS bound to Mitoxantrone similarly as heparin, but chondroitin sulfate (CS) did not bind to Mitoxantrone significantly (Figure 5D). Moreover, Banoxantrone, an anti-cancer drug structurally related to Mitoxantrone did not show significant interaction with either heparin or HS (Figure 5E, Fig. S4D, E). These results suggest a specific and direct interaction between Mitoxantrone and HS, which explains the SLC35B2-dependent association with the cell membranes. Importantly, compared to Mitoxantrone, Banoxantrone was a much weaker SARS-CoV-2 PP entry inhibitor (Figure 5F), suggesting a crucial role for heparin/HS binding in the anti-viral activity of Mitoxantrone.

Although Mitoxantrone binds HS directly, it did not disrupt the binding of SARS-CoV-2 PP to ACE2-GFP-expressing cells. Instead, when cells pretreated with Mitoxantrone were exposed to SARS-CoV-2 PP, most viral particles remained bound to the plasma membrane as revealed by immunostaining with an anti-Spike antibody (Figure 5G). By contrast, in control cells, Spike antibodies detected mostly intracellular speckles, probably representing endocytosed viral particles (Figure 5G). This result suggests that Mitoxantrone and Spike bind HS in different modes, but the binding of Mitoxantrone to HS alters its function to block viral entry.

Surprisingly, while weaker inhibitors like BNTX rescued the CPE of SARS-CoV-2 in Vero E6 cells, Mitoxantrone did not show any activity in this assay. This might be due to cytotoxicity linked to the DNA binding off-target property of Mitoxantrone. Consistent with this notion, Vero E6 cells were more sensitive to Mitoxantrone-induced cell death (Fig. S4F vs. Figure 5A). In this regard, it is compelling to see that the dose-dependent toxicity profiles of Mitoxantrone and Banoxantrone were indistinguishable (Fig. S4F), which suggests the

10

possibility of generating Mitoxantrone derivatives with reduced cytotoxicity but similar antiviral activity.

A combination regimen optimally targeting the HS-assisted viral entry

We next used gene expression profiling to further define the action of Tilorone, Raloxifene, and Piceatannol in comparison to Mitoxantrone. We treated HEK293T cells with these drugs at a dose that inhibited Spike-mediated viral entry. Differential gene expression analyses showed that Mitoxantrone had the most significant impact on gene expression, probably due to its strong DNA binding activity (Figure 6A). By contrast, Tilorone had the smallest effect, altering a limited number of genes by only small changes (Fig. S5A-D). Cluster analysis showed that the gene expression signature associated with Raloxifene treatment was more similar to that of Piceatannol-treated cells than to Tilorone-treated cells (Figure 6A), consistent with the observation that Raloxifene and Piceatannol but not Tilorone interact with heparin.

Conceptually, it might be possible to combine drugs targeting distinct steps in the HS-assisted entry pathway to produce synergized anti-viral activity. We tested the combination of Raloxifene with Tilorone because the latter has been used as an anti-viral agent and because either Tilorone or Raloxifene by itself modestly rescued SARS-CoV-2-induced CPE in Vero E6 cells (Fig. S5E, F). Strikingly, co-treatment with 1.5 μM Raloxifene reduced IC_{50} of Tilorone by ~10-fold in the CPE assay (Figure 6B). The synergistic inhibition of viral CPE was further confirmed by a matrix test, in which Tilorone was tested systematically with different concentrations of Raloxifene (Figure 6C). Importantly, no significant cytotoxicity was observed in combined treatment even at highest concentrations (Figure 6D).

11

Discussion

It is known that ACE2-mediated SARS-CoV and CoV-2 entry is controlled by a protease-dependent priming step [14-16]. Evidence presented in this study supports an additional layer of regulation imposed by the cell surface HS. The cell surface HS proteoglycans comprise of two protein families (6 Glypicans and 4 Syndecans) [32]. Proteins of these two families share no sequence similarity, but they all bear negatively charged HS polymers that can promote cell interactions with a variety of endocytic ligands [20, 21]. Our data together with recent preprints in BioRxiv support a model in which HS glycans help to recruit SARS-CoV-2 to the cell surface, which increases its local concentration for effectively engaging ACE2 [43, 44] (Figure 6E). Interestingly, some other coronaviruses also use a similar two-receptor mechanism for cell entry. For example, some α-Coronaviruses first attach themselves to sialoglycans on the cell surface before binding to proteinaceous receptors [45, 46].

How do HS glycans interact with Spike? Two recent studies posted at BioRxiv modeled the interactions of heparin with Spike using either full length Spike or just the RBD domain [29, 44]. While several potential binding sites were suggested on full length Spike, a more sensible model was generated when the RBD domain was used. This model suggests a long positive charge-enriched binding groove that accommodates a chain of heparin/HS. This model, if confirmed, is consistent with the observed salt sensitive heparin-Spike interaction.

How Mitoxantrone inhibits SARS-CoV and CoV-2 entry remains to be elucidated. It is known that Spike in the prefusion state adopts distinct conformations with the RBD domain either in the up or down position [44, 47], and the interaction of Spike with ACE2 requires the RBD-up conformation [11, 48-50]. By contrast, the proposed HS binding model is compatible with either the RBD-up or down conformation [44]. Thus, it is possible that HS binding occurs on Spike with

12

flexible RBD positions, and this conformational plasticity may facilitate downstream steps such as ACE2-dependent endocytosis and/or protease-mediated priming [51]. Mitoxantrone might influence the way HS interacts with the Spike and thus inhibits viral entry.

In addition to Mitoxantrone, we uncover several other drugs capable of targeting HS and HS-dependent endocytosis. The fact that many of these drugs also mitigate Spike-dependent viral entry strongly corroborates the idea that ACE2-mediated endocytosis serves a major role in SARS-CoV-2 cell entry. The identified drugs have a relatively limited impact on endocytosis as they affect neither clathrin-mediated transferrin uptake nor clathrin-independent uptake of CTB. Thus, these drugs are expected to be less toxic than previously reported pan-endocytosis inhibitors [13]. Among the drug identified, Sunitinib and BNTX disrupt actin dynamics (Figure 7E), suggesting the actin network as a previously unknown regulator for SARS-CoV and CoV-2 entry. These viruses may enter cells using receptor-mediated macropinocytosis, which depends on actin and has been known for its role in in viral pathogen uptake [52].

Although our study focuses on SARS-CoV and CoV-2, drugs targeting HS and HS-dependent endocytosis are expected to have a broad antiviral activity. Consistent with this view, Tilorone has long been recognized as a general antiviral agent. An early study in mice suggested that Tilorone administrated orally might upregulate interferon production [53], but our gene expression study did not reveal significant changes in the expression of interferon by Tirolone treatment. Instead, the demonstration of Tilorone as an inhibitor of HS-dependent endocytosis offers an alternative explanation for the reported antiviral function. Importantly, our study also suggests that Raloxifene, a heparin/HS-binding drug can enhance the anti-viral activity of Tilorone. Raloxifene is a selective estrogen receptor modulator used to treat osteoporosis and to prevent breast cancer in postmenopausal women (drugbank.ca/drugs/DB00481) [54]. Both Tilorone

and Raloxifene are well tolerated and can be conveniently administrated orally. Thus, whether this combination can be clinically effective against SARS-CoV-2 infection deserves additional testing in animal and other anti-viral models. In summary, our study not only establishes HS-dependent viral entry as a novel drug target for COVID-19, but also reveals candidate drugs that disrupt this critical event in the SARS-CoV-2 life cycle.

Methods

Chemicals and reagents

The initial screening library LOPAC[R1280] was purchased from Sigma. The chemicals for the follow-up studies were purchased as indicated in the table below. Standard quality control by HPLC was conducted before the drugs were used in the study. pcDNA3.1-SARS-CoV2-Spike plasmid was obtained from BEI resource [11]. Other chemicals and reagents were listed in the table below.

Cell line, transfection, lentivirus production, and infection

HEK293T cells stably expressing human ACE2 tagged with GFP (ACE2-GFP) were generated by transfecting cells with pCMV-ACE2-GFP (Covex), and stable clones were hand-picked after neomycin (1 mg/ml) selection for 1 week. Two ACE2-GFP cell lines using either HEK293 or HEK293T as the parental line were independently generated and used at NCATS and NIDDK, respectively. U2OS cells stably expressing Clathrin light chain-mCherry and Tractin-EGFP and the CRISPRv2 construct expressing sgRNA targeting *SLC35B2* were described previously [19]. Calu-3 cells were purchased from ATCC and maintained in MEM with 10% fetal bovine serum. sgRNA-expressing lentiviruses were produced by transfecting 1 million 293FT cells (Thermo

Fisher Scientific) in a 3.5 cm dish with 0.4 µg pVSV-G, 0.6 µg psPAX2, and 0.8 µg CRISPRv2-sgRNA. Transfected cells were incubated with 3 ml fresh DMEM medium for 72 h before viruses were harvested.

α-Synuclein fibrils uptake assay and drug screen

Fluorescence dye labeled α-Syn preformed fibrils were generated as previously described [19]. siRNA-mediated gene silencing was performed by lipofectamine RNAiMAX (Invitrogen) mediated transfection following the instruction from the manufacture. HEK293T cells were seeded in white 1,536-well microplates that have transparent bottom (Greiner BioOne) at 2,000 cells/well in 2 µL media and incubated at 37 °C overnight (~16 h). pHrodo red-labeled α-Syn fibrils were added at 400 nM final concentration to each well by a dispenser. After 1 h incubation, compounds from the LOPAC[R1280] library (Sigma) were titrated 1:3 in DMSO and dispensed via pintool at 23 nl/well to the assay plates. After 24 hours of incubation, the fluorescence intensity of pHrodo red was measured by a CLARIOstar Plus plate reader (BMG Labtech). Data were normalized using cells containing 400 nM pHrodo red-labeled Syn fibrils as 100% and medium containing 400 nM preformed fibrils-pHrodo red as 0%.

SARS-CoV and SARS-CoV-2 pseudotyped particles (PP)

SARS-CoV-S, SARS-CoV2-S, and ΔEnv (lack the Spike protein) pseudotyped particles (PP) were custom manufactured by the Codex Biosolutions (Gaithersburg, MD) following previously reported methods using a murine leukemia virus (MLV) pseudotyping system [55, 56]. The SARS-CoV2-S construct with Wuhan-Hu-1 sequence (BEI #NR-52420) was C-terminally truncated by 19 amino acids to reduce ER retention for pseudotyping [12].

15

PP entry assay in the 1536-well format

HEK293-ACE2 cells seeded in white, solid bottom 1536-well microplates (Greiner BioOne) at 2,000 cells/well in 2 µL medium were incubated at 37 °C with 5% CO2 overnight (~16 h). Compounds were titrated 1:3 in DMSO and dispensed via pintool at 23 nl/well to the assay plates. Cells were incubated with compounds for 1 h at 37 °C with 5% CO_2 before 2 µl/well of PP were added. The plates were then spinoculated by centrifugation at 1,500 rpm (453 x g) for 45 min and incubated for 48 h at 37 °C 5% CO2 to allow cell entry of PP and the expression of luciferase. After the incubation, the supernatant was removed with gentle centrifugation using a Blue Washer (BlueCat Bio). Then 4 µL/well of Bright-Glo luciferase detection reagent (Promega) was added to assay plates and incubated for 5 min at room temperature. The luminescence signal was measured using a PHERAStar plate reader (BMG Labtech). Data were normalized with wells containing PP as 100% and wells containing control ΔEnv PP as 0%. Experiments shown in Figure 4A-C, Fig. S3A, Figure 5A were conducted in this format at NCATS.

PP entry assay in the 96-well format

HEK293T-ACE2-GFP cells were seeded in white, transparent bottom 96-well microplates (Thermo Fisher Scientific) at 20,000 cells per well in 100 µl growth medium and incubated at 37 °C with 5% CO2 overnight (~16 h). The growth medium was carefully removed and 50 µl PP or PP containing compounds were added into each well. The plates were then spinoculated by centrifugation at 1500 rpm (453 x g) for 45 min and incubated for 24h (48 h for Calu-3 cells) at 37 °C 5% CO_2 to allow cell entry of PP and the expression of luciferase. After incubation, the supernatant was carefully removed. Then 50 µl/well of Bright-Glo luciferase detection reagent

(Promega) was added to assay plates and incubated for 5 min at room temperature. The luminescence signal was measured by a Victor 1420 plate reader (PerkinElmer). For ACE2-GFP cells, the GFP signal was also determined by the plate reader. Data were normalized with wells containing PP but no compound as 100%, and wells mock-treated with phosphate buffer saline (PBS) as 0%, and the ratio of luciferase to the corresponding GFP intensity was calculated. Experiments shown in Figure 1B, D, Figure 2B, C, Figure 5F were done following this protocol at NIDDK.

ATP content cytotoxicity assay in the 1536-well format

HEK293-ACE2 cells were seeded in white, solid bottom 1,536-well microplates (Greiner BioOne) at 2,000 cells/well in 2 µl medium and incubated at 37 °C with 5% CO2 overnight (~16 h). Compounds were titrated 1:3 in DMSO and dispensed via pintool at 23 nl/well to assay plates. Cells were incubated for 1 h at 37 °C 5% CO2 before 2 µl/well of media was added. The plates were then incubated at 37 °C for 48 h at 37C 5% CO2. After incubation, 4 µl/well of ATPLite (PerkinElmer) was added to assay plates and incubated for 15 min at room temperature. The luminescence signal was measured using a Viewlux plate reader (PerkinElmer). Data were normalized with wells containing cells as 100%, and wells containing media only as 0%.

ATP content cytotoxicity assay in the 96-well format

HEK293T-ACE2-GFP cells were seeded in white, transparent bottom 96-well microplate (Thermo Fisher Scientific) at 20,000 cells per well in 100 µl/well growth medium and incubated at 37 °C with 5% CO2 overnight (~16 h). The growth medium was carefully removed and 100 µl medium with compounds was added into each well. The plates were then incubated at 37 °C

17

for 24 h (48 h for Calu3 cells) at 37 °C 5% CO2. After incubation, 50 μL/well of ATPLite (PerkinElmer) was added to assay plates and incubated for 15 min at room temperature. The luminescence signal was measured using a Victor plate reader (PerkinElmer). Data were normalized with wells containing cells but no compound as 100%, and wells containing media only as 0 %.

SARS-CoV-2 cytopathic effect (CPE) assay

SARS-CoV-2 CPE assay was conducted at the Southern Research Institute (Birmingham, AL) as fee-for-service. Briefly, compounds were titrated in DMSO and acoustically dispensed into 384-well assay plates at 60 nl/well. Cell culture medium (MEM, 1% Pen/Strep/GlutaMax, 1% HEPES, 2% HI FBS) was dispensed at 5 μl/well into assay plates and incubated at room temperature. Vero E6 (selected for high ACE2 expression) was inoculated with SARS CoV-2 (USA_WA1/2020) at 0.002 M.O.I. in media and quickly dispensed into assay plates at 4,000 cells/well in 25 μl volume. Assay plates were incubated for 72 h at 37 °C, 5% CO$_2$, 90% humidity. Then, 30 μl/well of CellTiter-Glo (Promega) was dispensed, incubated for 10 min at room temperature, and the luminescence signal was read on an EnVision plate reader (PerkinElmer). An ATP content cytotoxicity assay was conducted with the same protocol as CPE assay except that SARS-CoV-2 virus was omitted from the incubation.

GFP+ purification and HSPG staining

His-tagged GFP+ was reported previously [19]. To stain the cell surface HSPG by GFP+, we incubated cells with 200 nM GPF+ in the growth medium on ice for 15min. Cells were then fixed and stained with DAPI to reveal the nucleus.

Endocytosis and viral binding assays

To test the effect of the compounds on DNA uptake, we seeded HEK293T cells previously infected with a YFP-expressing retrovirus at 0.2 x 10^6/well in a poly-lysine D coated 12 well plate. 24 h later, cells were treated with the chemicals for 30 min before a transfection mixture containing 0.2 µg mCherry-expressing plasmid and 0.6 µl TransIT293 (Mirus) was added to the cells. Cells were incubated with the DNA for 4 h, after which the medium was replenished. The cells were further grown for 48 h. Cells were then lysed in NP40 lysis buffer and the fluorescence intensity in cleared lysates was measured by a Fluoromax3 fluorometer (Horiba).

To test the effect of compounds on VSVG-coated lentivirus uptake/infection, HEK293T cells expressing YFP were seeded at 0.2x10^6/well in a poly-lysine D coated 12 well plate. After 24 h, cells were treated with compounds for 30 min and then infected with a mCherry-expressing lentivirus at M.O.I. of ~ 2.0 in the presence of the compounds for 6 h. The virus and compounds were removed, and cells were further grown in fresh medium for 48 h before fluorescence measurement.

To test the effect of compounds on GFP+ or transferrin uptake, HEK293T cells were seeded at 25,000 cells per well in an 8 well chamber (ibidi). 24 h later, cells were treated with compounds for 30 min before the addition of GFP+ (200 nM) or transferrin (Thermo Fisher Scientific) (50 µg/ml). Cells were further incubated at 37 °C for 4 h before fixation and confocal imaging.

To detect the binding of SARS-CoV-2 to the cell surface, HEK293T-ACE2-GFP cells seeded in 24 well plates that had been coated with fibronectin were treated with 50 µl virus per well at 4 °C for 1 h with centrifugation at 1500 rpm (453 x g) for 60 min. Cells were carefully

19

washed with ice-cold PBS to remove unbound virus and then lysed in a NP40 lysis buffer containing 0.5 % Igepal, 20 mM Tris pH 7.4, 150 mM Sodium Chloride, 2 mM Magnesium Chloride, 0.5 mM EDTA, 1 mM DTT, and a protease inhibitor cocktail. The cell extracts cleared by centrifugation (16,000 x g 5 min) were analyzed by immunoblotting.

UPLC-MS/MS assay

Ultra-performance liquid chromatography-tandem mass spectrometry (UPLC-MS/MS) methods were developed and optimized to determine compounds' concentrations in the in vitro samples. Mass spectrometric analysis was performed on a Waters Xevo TQ-S triple quadrupole instrument using electrospray ionization in positive mode (Mitoxantrone, BNTX, Tilorone and Sunitinib) and negative mode (Raloxifene, Piceatannol, Exifone, K114) with the selected reaction monitoring. The separation of test compounds was performed on an Acquity BEH C_{18} column (50 x 2.1 mm, 1.7 μ) using a Waters Acquity UPLC system with 0.6 mL/min flow rate and 2 minute gradient elution. The mobile phases were 0.1% formic acid in water and 0.1% formic acid in acetonitrile. The calibration standards (0.100 – 100 μM) and quality control samples were prepared in 50% acetonitrile/water with 0.1% formic acid and PBS buffer. Aliquots of 10 μL samples were mixed with 200 μL internal standard in acetonitrile to precipitate proteins in a 96-well plate. 0.5 μL supernatant was injected for the UPLC-MS/MS analysis. Data were analyzed using MassLynx V4.1 (Waters Corp., Milford, MA).

qRT-PCR analysis of knockout or knockdown cells

Total RNA was extracted from 3 million HEK293T cells using TriPure reagent (Roche) and purified using RNeasy MinElute Cleanup Kit (Promega) following the standard protocols. The

20

RNA concentration was measured by Nanodrop 2000 UV spectrophotometer, and 1µg total RNA was converted to cDNA using the iScript Reverse Transcription Supermix (BioRad) system. 1µL cDNA was used to perform qPCR using SsoAdvanced SYBR Green supermix kit (BioRad) on a CFX96 machine (BioRad). Data were analyzed using BioRad CFX Manager 3.0 software. GADPH was used as a reference gene for the quantification of gene expression levels. Primers used for qRT-PCR were listed in the previous study [19]. For the RNAseq study, cells were treated independently for 6 h with each drug three times and 6 untreated control samples were included. The treatment conditions are Mitoxantrone 5 µM, Tilorone 10 µM, Raloxifene 10 µM, Piceatannol 10 µM. RNA isolated from control or drug-treated cells (10 µg/sample) were processed by Novagene USA.

Membrane fractionation and heparin Sepharose pulldown

To fractionate cells, ~15 million cells were treated with 5 µM Mitoxantrone or Banoxantrone for 30 min at 37 °C. Cells were harvested and washed with ice-cold PBS. Cells were then resuspended and incubated in 900 µl of a hypotonic buffer (50 mM HEPES, pH 7.3, 25 mM potassium acetate) containing a protease inhibitor cocktail. Cells were homogenized in a Dounce homogenizer with a tight pestle and then subject to differential centrifugation at 1,000 g for 5 min, 7,000 x g for 10min, and 100,000 x g for 20 min. The P100 membrane pellet was resuspended in 20 µl NP40 lysis buffer containing 20 mM Tris pH 7.4, 0.5% NP40, 150 mM Sodium Chloride, 2 mM Magnesium Chloride. The absorbance in the cleared membrane extract and the S100 fraction was measured by a NanoDrop 2000 spectrometer. Note that no absorbance was detected for the S100 fraction even when the samples were measured by a conventional spectrometer with a 10 x light path.

21

To determine the binding of Mitoxantrone to heparin-coated Sepharose, the compound was diluted to 50 µM in PBS and then incubated with PBS-washed heparin beads or as a control with Sepharose. After brief mixing, the beads were sedimented by centrifugation. The supernatant fractions were analyzed by NanoDrop 2000 for light absorption at the wavelengths specified in the figure legends.

The pulldown of Spike by heparin beads were done by incubating 600ng Spike with pre-washed heparin Sepharose in 25mM Tris pH 7.3, 2mM KCl, 1mM $MgCl_2$, 0.05% Igepal with or without 150mM NaCl. To test the effect of Mitoxantrone on heparin-Spike interaction, 30 µl heparin beads were washed with PBS, treated with 200 µl Mitoxantrone (100 µM) for 5 min at room temperature or as a control remained untreated. Unbound Mitoxantrone was removed after centrifugation. The beads were then incubated with 600 ng purified Spike protein in 300 µl PBS containing 0.05% NP40 and 1mM DTT. The reaction was incubated at room temperature for 30 min. The beads were washed two times with PBS and eluted with 1 x Laemmli buffer for SDS-PAGE and immunoblotting analysis.

Drug synergy analysis

CPE and Toxicity were normalized using independent control wells (DMSO ± virus) on each plate, so activity values were not strictly bounded between [0, 100]. For CPE assay, DMSO+virus was treated as the neutral control, whereas DMSO-only (no virus) served as the positive control. Then normalized CPE = 1 - (x - neutralCtrl) / (positiveCtrl - neutralCtrl) × 100%. For viability assay, DMSO-only was used as the neutral control and media-only wells (no cell) as the negative control. Normalized viability = (x - negativeCtrl) / (neutralCtrl -

negativeCtrl) $\times$ 100%. Synergism and antagonism from a 6×6 block were evaluated using the highest single agent model (HSA). Given a dose combination $A_{conc1} + B_{conc2}$,

$$HSA(A_{conc1}+B_{conc2}) = activity(A_{conc1}+B_{conc2}) - MIN[activity(A_{conc1}), activity(B_{conc2})]$$

Therefore, we have

Synergism: $HSA(*) < 0$ (value from combination is lower than the best single agent)

Antagonism: $HSA(*) > 0$ (value from combination is greater than the best single agent)

Additivity: $HSA(*) = 0$ (value from combination equals to best single agent)

The overall HSA synergism (HSA_{sum}) given a 6×6 block was calculated as the sum of $HSA(A_{conc*}+B_{conc*})$ across the non-toxic dose combinations (defined as viability activity > 80). We used empirical cutoff $HSA_{sum} < -100$ to call a synergistic combination. The highest concentration of Raloxifene was excluded from the figure because it alone induced significant cytotoxicity.

Image processing and statistical analyses

Confocal images were processed using the Zeiss Zen software. To measure fluorescence intensity, we used the Fiji software. Images were converted to individual channels and region of interest was drawn for measurement. Statistical analyses were performed using either Excel or GraphPad Prism 8. Data are presented as mean $\pm$ SEM, which was calculated by GraphPad Prism 8. *p*-values were calculated by Student's t-test using Excel. None linear curve fitting and IC_{50} calculation was done with GraphPad Prism 8 using the inhibitor response 3 variable model or the exponential decay model. Images were prepared with Adobe Photoshop and assembled in Adobe Illustrator. All experiments presented were repeated at least twice independently except

for the data from the Southern Research Institute, which was performed as fee-for-service in 2 duplicates. Data processing and reporting are adherent to the community standards.

Data Availability

All data, associated protocols, methods, and sources of materials can be accessed in the main text or supplementary information. The analysis code for drug synergy study is available at NCATS github. The mRNA sequencing data has been deposited to NCBI Sequence Read Archive. The accession ID is: PRJNA645209.

Acknowledgements

Author contribution

Q. Zhang, M. Swaroop, W. Zheng, and Ye, Y. designed the drug screen, Q. Zhang, C. Chen, Y. Xu, W. Zheng, and Ye Y. conceived and designed the study, A.Q. Wang, X. Xu, and C. Chen designed the mass spectrometry experiment, Q. Zhang, C. Chen, Y. Xu, W. Zheng, L. Chen, A.Q. Wang, and Ye Y. analyzed the data. Q. Zhang, M. Swaroop, M. Pradhan, M. Xu, L. Wang, J. Lee, M. Shen, Z. Luo, W. Huang, A.Q. Wang, X. Xu, N. Hagen, and Y. Ye conducted

the experiments. Y. Ye wrote the manuscript. All authors contribute to the editing of the manuscript.

Competing financial interests

The authors declare no competing financial interests.

References

1 Zhou P, Yang XL, Wang XG *et al.* A pneumonia outbreak associated with a new coronavirus of probable bat origin. *Nature* 2020; **579**:270-273.

2 Zhu N, Zhang D, Wang W *et al.* A Novel Coronavirus from Patients with Pneumonia in China, 2019. *N Engl J Med* 2020; **382**:727-733.

3 Holmes KV. SARS-associated coronavirus. *N Engl J Med* 2003; **348**:1948-1951.

4 Marsh M, Helenius A. Virus entry: open sesame. *Cell* 2006; **124**:729-740.

5 Tortorici MA, Veesler D. Structural insights into coronavirus entry. *Adv Virus Res* 2019; **105**:93-116.

6 Wang H, Yang P, Liu K *et al.* SARS coronavirus entry into host cells through a novel clathrin- and caveolae-independent endocytic pathway. *Cell Res* 2008; **18**:290-301.

7 Burkard C, Verheije MH, Wicht O *et al.* Coronavirus cell entry occurs through the endo-/lysosomal pathway in a proteolysis-dependent manner. *PLoS Pathog* 2014; **10**:e1004502.

8 Belouzard S, Millet JK, Licitra BN, Whittaker GR. Mechanisms of coronavirus cell entry mediated by the viral spike protein. *Viruses* 2012; **4**:1011-1033.

9 Inoue Y, Tanaka N, Tanaka Y *et al.* Clathrin-dependent entry of severe acute respiratory syndrome coronavirus into target cells expressing ACE2 with the cytoplasmic tail deleted. *J Virol* 2007; **81**:8722-8729.

10 Glebov OO. Understanding SARS-CoV-2 endocytosis for COVID-19 drug repurposing. *FEBS J* 2020.

11 Walls AC, Park YJ, Tortorici MA, Wall A, McGuire AT, Veesler D. Structure, Function, and Antigenicity of the SARS-CoV-2 Spike Glycoprotein. *Cell* 2020; **181**:281-292 e286.

12 Ou X, Liu Y, Lei X *et al.* Characterization of spike glycoprotein of SARS-CoV-2 on virus entry and its immune cross-reactivity with SARS-CoV. *Nat Commun* 2020; **11**:1620.

13 Kang YL, Chou YY, Rothlauf PW *et al.* Inhibition of PIKfyve kinase prevents infection by EBOV and SARS-CoV-2. *bioRxiv* 2020.

14 Hoffmann M, Kleine-Weber H, Schroeder S *et al.* SARS-CoV-2 Cell Entry Depends on ACE2 and TMPRSS2 and Is Blocked by a Clinically Proven Protease Inhibitor. *Cell* 2020; **181**:271-280 e278.

15 Hoffmann M, Kleine-Weber H, Pohlmann S. A Multibasic Cleavage Site in the Spike Protein of SARS-CoV-2 Is Essential for Infection of Human Lung Cells. *Mol Cell* 2020; **78**:779-784 e775.

16 Shang J, Wan Y, Luo C *et al.* Cell entry mechanisms of SARS-CoV-2. *Proc Natl Acad Sci U S A* 2020; **117**:11727-11734.

17 Millet JK, Whittaker GR. Physiological and molecular triggers for SARS-CoV membrane fusion and entry into host cells. *Virology* 2018; **517**:3-8.

18 Zang R, Gomez Castro MF, McCune BT *et al.* TMPRSS2 and TMPRSS4 promote SARS-CoV-2 infection of human small intestinal enterocytes. *Sci Immunol* 2020; **5**.

19 Zhang Q, Xu Y, Lee J *et al.* A myosin-7B-dependent endocytosis pathway mediates cellular entry of alpha-synuclein fibrils and polycation-bearing cargos. *Proc Natl Acad Sci U S A* 2020; **117**:10865-10875.

20 Christianson HC, Belting M. Heparan sulfate proteoglycan as a cell-surface endocytosis receptor. *Matrix Biol* 2014; **35**:51-55.

21 Cagno V, Tseligka ED, Jones ST, Tapparel C. Heparan Sulfate Proteoglycans and Viral Attachment: True receptors or adapation Bias? *Viruses* 2020; **11**:596.

22 Milewska A, Zarebski M, Nowak P, Stozek K, Potempa J, Pyrc K. Human coronavirus NL63 utilizes heparan sulfate proteoglycans for attachment to target cells. *J Virol* 2014; **88**:13221-13230.

23 Milewska A, Nowak P, Owczarek K *et al.* Entry of Human Coronavirus NL63 into the Cell. *J Virol* 2018; **92**.

24 Lang J, Yang N, Deng J *et al.* Inhibition of SARS pseudovirus cell entry by lactoferrin binding to heparan sulfate proteoglycans. *PLoS One* 2011; **6**:e23710.

25 Naskalska A, Dabrowska A, Szczepanski A, Milewska A, Jasik KP, Pyrc K. Membrane Protein of Human Coronavirus NL63 Is Responsible for Interaction with the Adhesion Receptor. *J Virol* 2019; **93**.

26 Karpowicz RJ, Jr., Trojanowski JQ, Lee VM. Transmission of alpha-synuclein seeds in neurodegenerative disease: recent developments. *Lab Invest* 2019; **99**:971-981.

27 Jeon S, Ko M, Lee J *et al.* Identification of antiviral drug candidates against SARS-CoV-2 from FDA-approved drugs. *Antimicrob Agents Chemother* 2020.

28 Mycroft-West C, Su D, Elli S *et al.* The 2019 coronavirus (SARS-CoV-2) surface protein (Spike) S1 Receptor Binding Domain undergoes conformational change upon heparin binding. *bioRxiv* 2020.

29 Kim SY, Jin W, Sood A *et al.* Characterization of heparin and severe acute respiratory syndrome-related coronavirus 2 (SARS-CoV-2) spike glycoprotein binding interactions. *Antiviral Res* 2020:104873.

30 Liu L, Chopra P, Li X, Wolfert MA, Tompkins SM, Boons GJ. SARS-CoV-2 spike protein binds heparan sulfate in a length- and sequence-dependent manner. *bioRxiv* 2020.

31 de Haan CA, Haijema BJ, Schellen P *et al.* Cleavage of group 1 coronavirus spike proteins: how furin cleavage is traded off against heparan sulfate binding upon cell culture adaptation. *J Virol* 2008; **82**:6078-6083.

32 Sarrazin S, Lamanna WC, Esko JD. Heparan sulfate proteoglycans. *Cold Spring Harb Perspect Biol* 2011; **3**.

33 Meneghetti MC, Hughes AJ, Rudd TR *et al.* Heparan sulfate and heparin interactions with proteins. *J R Soc Interface* 2015; **12**:0589.

34 Song Y, Thiagarajah J, Verkman AS. Sodium and chloride concentrations, pH, and depth of airway surface liquid in distal airways. *J Gen Physiol* 2003; **122**:511-519.

35 Park RJ, Wang T, Koundakjian D *et al.* A genome-wide CRISPR screen identifies a restricted set of HIV host dependency factors. *Nat Genet* 2017; **49**:193-203.

36 Wernick NL, Chinnapen DJ, Cho JA, Lencer WI. Cholera toxin: an intracellular journey into the cytosol by way of the endoplasmic reticulum. *Toxins (Basel)* 2010; **2**:310-325.

37 Ekins S, Madrid PB. Tilorone, a Broad-Spectrum Antiviral for Emerging Viruses. *Antimicrob Agents Chemother* 2020; **64**.

38 Le Tourneau C, Raymond E, Faivre S. Sunitinib: a novel tyrosine kinase inhibitor. A brief review of its therapeutic potential in the treatment of renal carcinoma and gastrointestinal stromal tumors (GIST). *Ther Clin Risk Manag* 2007; **3**:341-348.

39 Melak M, Plessner M, Grosse R. Actin visualization at a glance. *J Cell Sci* 2017; **130**:525-530.

40 Kouznetsova J, Sun W, Martinez-Romero C *et al.* Identification of 53 compounds that block Ebola virus-like particle entry via a repurposing screen of approved drugs. *Emerg Microbes Infect* 2014; **3**:e84.

41 Kapuscinski J, Darzynkiewicz Z. Interactions of antitumor agents Ametantrone and Mitoxantrone (Novatrone) with double-stranded DNA. *Biochem Pharmacol* 1985; **34**:4203-4213.

42 Crespi MD, Ivanier SE, Genovese J, Baldi A. Mitoxantrone affects topoisomerase activities in human breast cancer cells. *Biochem Biophys Res Commun* 1986; **136**:521-528.

43 Tandon R, Sharp JS, Zhang F *et al.* Effective Inhibition of SARS-CoV-2 Entry by Heparin and Enoxaparin Derivatives. *bioRxiv* 2020.

44 Clausen TM, Sandoval DR, Spliid CB *et al.* SARS-CoV-2 Infection Depends on Cellular Heparan Sulfate and ACE2. *bioRxiv* 2020.

45 Liu C, Tang J, Ma Y *et al.* Receptor usage and cell entry of porcine epidemic diarrhea coronavirus. *J Virol* 2015; **89**:6121-6125.

46 Schwegmann-Wessels C, Zimmer G, Schroder B, Breves G, Herrler G. Binding of transmissible gastroenteritis coronavirus to brush border membrane sialoglycoproteins. *J Virol* 2003; **77**:11846-11848.

47 Cai Y, Zhang J, Xiao T *et al.* Distinct conformational states of SARS-CoV-2 spike protein. *Science* 2020.

48 Lan J, Ge J, Yu J *et al.* Structure of the SARS-CoV-2 spike receptor-binding domain bound to the ACE2 receptor. *Nature* 2020; **581**:215-220.

49 Yan R, Zhang Y, Li Y, Xia L, Guo Y, Zhou Q. Structural basis for the recognition of SARS-CoV-2 by full-length human ACE2. *Science* 2020; **367**:1444-1448.

50 Wrapp D, Wang N, Corbett KS *et al.* Cryo-EM structure of the 2019-nCoV spike in the prefusion conformation. *Science* 2020; **367**:1260-1263.

51 Henderson R, Edwards RJ, Mansouri K *et al.* Controlling the SARS-CoV-2 spike glycoprotein conformation. *Nat Struct Mol Biol* 2020.

52 Yamauchi Y, Helenius A. Virus entry at a glance. *J Cell Sci* 2013; **126**:1289-1295.

53 Mayer GD, Krueger RF. Tilorone hydrochloride: mode of action. *Science* 1970; **169**:1214-1215.

54 Riggs BL, Hartmann LC. Selective estrogen-receptor modulators -- mechanisms of action and application to clinical practice. *N Engl J Med* 2003; **348**:618-629.

55 Millet JK, Tang T, Nathan L *et al.* Production of Pseudotyped Particles to Study Highly Pathogenic Coronaviruses in a Biosafety Level 2 Setting. *J Vis Exp* 2019.

56 Millet JK, Whittaker GR. Murine Leukemia Virus (MLV)-based Coronavirus Spike-pseudotyped Particle Production and Infection. *Bio Protoc* 2016; **6**.

28

Figure 1 Heparin inhibits Spike-mediated SARS-CoV and CoV-2 entry.

(**A**) The chemical structures of heparan sulfate and heparin.

(**B**) The experimental scheme for inhibitor testing in HEK293T ACE2-GFP cells.

(**C**) Heparin mitigates the entry of SARS-CoV and SARS-CoV-2 pseudoviral particles (PP). ACE2-GFP HEK293T cells were transduced with SARS-CoV and SARS-CoV-2 PP in the presence of heparin as indicated. The ratio of luciferase vs. GFP was measured 24 h post-transduction. Error bars indicate SEM, N=4.

(**D**) Heparin interacts with Spike in a salt sensitive manner. Spike (600ng) was incubated with either control or heparin-conjugated beads in a buffer containing 0 or 150mM NaCl. Bound proteins were analyzed by SDS-PAGE and Coomassie blue staining. Note that a small amount of Spike interacts with heparin in the presence of 150mM NaCl.

Figure 2 Heparan sulfate promotes Spike-mediated SARS-CoV and CoV-2 entry

(**A**) The HSPG biosynthetic pathway. Genes chosen for knockdown or knockout (KO) are in red.

(**B**) Knockdown of *XYLT2* reduces SARS-CoV and SARS-CoV-2 PP entry. ACE2-GFP cells transfected with either control or *XYLT2* siRNA were transduced with SARS-CoV (grey) or SARS-CoV-2 (orange) PP for 24 h and the ratio of luciferase/GFP was determined. A parallel experiment done without the virus provides another control for the effect of gene knockdown on cell viability (blue). Error bars indicate SEM, N=4. **, $p<0.01$, ****, $p<0.0001$ by unpaired Student t-test.

(**C**) *SCL35B2* is required for SARS-CoV and SARS-CoV-2 cell entry. As in B, except that control and *SLC35B2* CRISPR KO cells were used.

29

(**D** and **E**) *SLC35B2* promotes the binding of SARS-CoV-2 PP to cells. (D) ACE2-GFP cells were spin-infected at 4 °C for 1 h. After washing, the virus bound to the cells was detected by immunoblotting. (E) The binding of SARS-CoV-2 PP to control and *SLC35B2* deficient cells was analyzed by immunoblotting. S and S2 indicate the full length and furin-cleaved S2 fragment, respectively.

Figure 3 Two classes of drugs targeting HS-dependent cargo entry.

(**A**) A high-throughput drug screen for inhibitors that block the uptake of fluorescently labeled α-Syn fibrils.

(**B**) A summary of the drugs identified. AC_{50} was calculated from the automated screen. IC_{50} was determined by a follow-up repeat shown in D.

(**C**) A heat map summary of the endocytosis inhibitory activity for the indicated drugs. All drugs were tested at 10 µM except for Sunitinib and Mitoxantrone (5 µM each). See Supplementary Figure 2 for details.

(**D**) Mass spectrometry analysis of drug binding to heparin beads. The indicated drugs were incubated with either control or heparin-conjugated beads. Unbound drugs were quantified by mass spectrometry. N=2. MTAN, Mitoxantrone.

Figure 4 The actin cytoskeleton is required for HS-assisted viral entry.

(**A**, **B**) Sunitinib and BNTX inhibit Spike-dependent entry of pseudoviral particles (PP). HEK293 ACE2-GFP cells were transduced with SARS-CoV and SARS-CoV-2 PP in the presence the indicated drugs. The luciferase expression was measured 48 h post-transduction. Error bars

indicate SEM, N=4. As a control for cytotoxicity, cells treated with the drugs without virus were analyzed in parallel by an ATP-based cytotoxicity assay.

(**C**) BNTX protects Vero E6 cells from SARS-CoV-2-induced cytopathic effect (CPE). Viability of Vero E6 cells was measured after treatment with the indicated drugs in the presence (black) or absence (red) of the SARS-CoV-2 virus. Error bars indicate SEM, N=2.

(**D** and **E**) Sunitinib stimulates actin filament formation at the cell periphery. (D) Confocal snapshots of a U2OS cell stably expressing Tractin-EGFP before or after Sunitinib (5 µM) treatment. The red arrows indicate new actin filaments formed in a direction perpendicular to the existing filaments. The inset shows an enlarged view of the box, which highlights newly formed filopodia. (E) Live cell imaging of actin filament formation after Sunitinib treatment (5 µM, 60min). The arrows indicate examples of actin filament assembly. The insets show an enlarged view of the boxed area. Scale bar, 5 µm.

(**F** and **G**) BNTX disrupts actin filaments at the cell periphery. (F) Confocal snapshots of a Tractin-EGFP cell before and after BNTX (10 µM) treatment. Arrows indicate the peripheral actin network disrupted by BNTX. (G) Live cell imaging shows the shrinking of peripheral membranes after BNTX treatment. Yellow arrowheads mark a retracting actin bundle.

(**H**) Latrunculin A inhibits SARS-CoV-2 entry. ACE2-GFP cells incubated with SARS-CoV-2 PP in the presence of Latrunculin A were analyzed for luciferase expression (Entry). A parallel treatment in the absence of the virus showed the toxicity of Latrunculin A (orange). Error bars indicate SEM. N=2. ***, $p<0.001$, ****, $p<0.0001$.

Figure 5 Mitoxantrone targets HS directly to inhibit SARS coronavirus entry.

(A) Mitoxantrone inhibits Spike-mediated entry of pseudoviral particles (PP). ACE2-GFP HEK293 cells were transduced with SARS-CoV and SARS-CoV-2 PP for 48 h in the presence of Mitoxantrone as indicated. Error bars indicate SEM, N=4. Cells treated without the virus were used to control drug cytotoxicity.

(B) The subcellular distribution of Mitoxantrone. The scheme illustrates the experimental procedure. HEK293T cells were treated with 5 µM Mitoxantrone for 30 min at 37 °C before fractionation. The membrane pellet (P100) and the cytosol supernatant (S100) fractions were analyzed by immunoblotting and by spectrometry at the indicated wavelengths. Error bars indicate SEM. N=3.

(C) The membrane association of Mitoxantrone requires *SLC35B2 (35B2)*. Cells of the indicated genotypes were treated with 5 µM Mitoxantrone for 30 min at 37 °C and then fractionated as in B. The absorbance of the P100 fractions was measured and the control sample at 680 nm was normalized to 1. Bottom panels show the cells stained with DAPI (blue) and GFP+ (green) to label DNA and HS (Green), respectively. Error bars indicate SEM. N=3.

(D) Mitoxantrone has a higher affinity for heparin and HS than chondroitin sulfate (CS). A_{650} of Mitoxantrone (5 µM) mixed with the indicated oligosaccharides was determined. The decrease in absorbance after the addition of the oligosaccharides was plotted. Error bars indicate SEM. N=2.

(E) The chemical structures and absorbance spectra of Mitoxantrone (MTAN) and Banoxantrone (BANO).

(F) Banoxantrone (BANO) has reduced antiviral activity. ACE2-GFP HEK293T cells were incubated with SARS-CoV-2 in the presence of the indicated drugs for 24 h before measuring the luciferase activity. Error bars indicate SEM. N=4.

(**G**) Mitoxantrone inhibits SARS-CoV-2 cell entry. ACE2-GFP HEK293T cells were pretreated with DMSO as a control or Mitoxantrone for 30 min before incubation with SARS-CoV-2 PP. Cells were fixed 3 h later and stained with anti-Spike antibodies (red) and DAPI (blue).

Figure 6 A combination regimen that optimally targets HS-dependent viral entry.

(**A**) A heatmap showing the gene expression profiles of untreated HEK293T cells or cells treated with the indicated drugs at 10 µM for 6 h (Mitoxantrone 5 µM).

(**B-D**) Drug combination studies show a synergistic CPE rescue effect by Tilorone and Raloxifene (Ralo.). (B) Vero E6 cells treated with Tilorone at different concentrations with (1.5 µM) or without Raloxifene were infected with SARS-CoV-2 for 72 h before viability test. Error bars indicate SEM. N=2. (C, D) Matrix blocks for Tilorone plus Raloxifene in the CPE and cell viability assays. Activity blocks show normalized levels of viral toxicity (C) or normalized cell viability (no virus) (D). Red labels in the synergy matrix indicate positive synergism whereas blue labels suggest antagonism.

(**E**) A SARS-CoV-2 entry map with the drug targeting sites identified in this study. PM, plasma membrane.

33

List of supplementary materials:

Table S1 A list of reagents used in the study

Figures S1-S6

Movies S1-S6

Supplementary Table S1

Reagents and Materials	Source	Catalogue No.
pHrodo™ Red, succinimidyl ester (pHrodo™ Red, SE)	ThermoFisher Scientific	Cat# P36600
Banoxantrone dihydrochloride	Sigma	Cat# SML1854
Heparin sodium salt from porcine intestinal mucosa	Sigma	Cat# H3393
Heparan sulfate sodium salt	Biosynth Carbosynth	YH30121
Chondroitin sulfate sodium salt	Biosynth Carbosynth	YH04273
SARS-CoV-S and SARS-CoV2-S Pseudotyped particles	Codex Biosolutions (Gaithersburg, MD)	Contracted custom production
ATPLite	PerkinElmer	Cat# 6016736
Bright-Glo Luciferase kit	Promega	Cat# E2620
CellTiter-Glo cell viability kit	Promega	Cat# G7572
iScript™ Reverse Transcription Supermix for RT-qPCR	BioRad	Cat# 1708840
SsoAdvanced Universal SYBR Green Supermix	BioRad	Cat# 1725271
Imaging chamber	iBidi	Cat# 80426
TriPure reagent	Sigma	Cat# 11667157001
RNeasy MinElute Cleanup Kit	Qiagen	Cat# 74024
Latrunculin A	TOCRIS	Cat# 3973
NCGC00015693-09	Microsource	01503278
NCGC00015889-11	Microsource	01505622
NCGC00024857-02	BIOMOL	AC-304
NCGC00094226-07	SigmaAldrich	Lopac-P-0453
NCGC00094226-13	Selleck	S3026
NCGC00095196-06	Microsource	02300009
NCGC00164631-05	Sequoia	SRP01785s
NCGC00186034-01	SigmaAldrich	Lopac-K-1015
NCGC00186034-03	SIGMA	K1015
NCGC00249050-02	GVK	FFS-12-73-NCI-3078
Spike S1_S2	Sino Biological	40589-V27B-B
pLV-mCherry	A gift from Pantelis Tsoulfas (Addgene #36084)	
pcDNA3.1-SARS-CoV2-Spike	BEI resources	NR-52420
SARS-CoV-2 S antibody	GeneTex	Cat# GTX632604

Figure 1 Establishing cell models to study Spike-dependent SARS coronavirus entry.

(**A, B**) The entry of SARS-CoV (C) or SARS-CoV-2 (D) PP in HEK293T ACE2-GFP cells. Uninfected cells or cells infected with the indicated PP for 24 h were analyzed for luciferase expression. The luciferase/GFP ratio was determined as an indicator of viral entry. Error bars indicate SEM. N=4.

(**C**) HEK293T cells or ACE2-GFP stable HEK293T cells were treated with SARS-CoV-2 PP as indicated. Luciferase expression was measured 48 post infection. Error bars indicate SEM. N=4.

(**D**) Cytotoxicity of heparin in HEK293T ACE2-GFP cells. Cell viability was measured 24 h after heparin treatment. Error bars indicate SEM. N=4.

(**E**) Heparin mitigates the entry of SARS-CoV and SARS-CoV-2 pseudoviral particles (PP) in Calu-3 cells. Calu-3 cells were transduced with SARS-CoV and SARS-CoV-2 PP in the presence of heparin as indicated. The luciferase levels were measured 48 h post-transduction. Error bars indicate SEM, N=4.

(**F**) Salt sensitive interaction of Spike with heparin. Spike (300 ng) or ACE2-mFC (300 ng) was incubated with heparin beads in the presence of salt as indicated. Proteins pulled down (PD) were analyzed by immunoblotting with anti-S2 antibodies. The graph shows the quantification of the experiment.

(**G**) Verification of *XYLT2* knockdown by qRT-PCR. A fraction of ACE2-GFP cells transfected with SMARTpooled *XYLT2* siRNAs or a control siRNA for 72 h were analyzed for *XYLT2* expression by qRT-PCR. The remaining cells were used in Figure 1F for viral entry and cell viability assay. Error bars indicate SEM, N=3 technical repeats.

36

(**H**) Generating ACE2-GFP cells deficient for *SLC35B2* (*35B2*). ACE2-GFP cells treated with *SLC35B2* sgRNA-expressing lentiviruses were incubated with Alex^{594}-labeled (400 nM) α-Syn fibrils for 4h. α-Syn negative *SLC35B2* knockout (KO) cells (dashed box) were identified and collected by FACS.

(**I**) Verification of *SLC35B2* knockdown by qRT-PCR. A fraction of ACE2-GFP cells transfected with SMARTpooled *SLC35B2* siRNAs or a control siRNA for 72 h were analyzed for *SLC35B2* expression by qRT-PCR. The remaining cells were used for viral entry and cell viability assay in Figure 1G. Error bars indicate SEM, N=3 technical repeats.

(**J**) The knockout of *SCL35B2* does not affect ACE2-GFP expression. The ACE2-GFP level in cell extracts used in Figure 2C was determined by a fluorometer.

Figure 2 Substrate specificity of the identified endocytosis inhibitors.

(A and B) Clathrin-independent endocytosis of cholera toxin B (CTB) chain is not affected by the identified drugs. (A) HEK2923T cells were treated with Mitoxantrone (5 µM) for 1h before incubation with 2 µg/ml Alexa^{555}-labeled CTB on ice for 15min (cell surface binding) or at 37 °C for 20min (uptake). Cells were fixed and stained with DAPI. Note that Mitoxantrone affects neither the binding of CTB to the cell surface nor its uptake. (B) Cells were treated with the indicated drugs at 10 µM (Sunitinib at 5 µM) for 1h before incubation with CTB at 37 °C for 20 min.

(**C**) The effect of drugs on the endocytosis of Transferrin. HEK293T cells were pretreated with the compounds for 30 min before incubation with Alexa^{488}-labeled Transferrin (50 µg/ml) at 37 °C for 4 h. Cells were fixed, stained with DAPI (blue), and imaged by confocal microscopy. The image shows an example of Transferrin uptake in control cells. The graph shows the

quantification of internalized Transferrin signal in individual cells. A.U., arbitrary unit. Error

bars indicate SEM.

(**D**) The effect of drugs on the endocytosis of GFP+. HEK293T cells treated with the indicated

compounds for 30 min were incubated with 100 nM GFP+ for 4 h before heparin wash, fixation,

and staining with Hoechst (Blue). The graph shows internalized GFP+ signals in individual cells.

The image shows an example of GFP+ uptake in control cells. A.U. arbitrary units. Error bars

indicate SEM. N=2.

(**E**) The effect of drugs on the entry of VSVG-pseudotyped lentivirus bearing a mCherry reporter.

HEK293T cells stably expressing YFP were treated with the inhibitors as in C, infected with

VSVG-Lenti-mCherry in the presence of the inhibitors for 6 h. Cells were then incubator in

virus-free, inhibitor-free medium for 48 h before quantification of the mCherry /YFP ratio by a

fluorometer. Error bars indicate SEM. N=4.

(**F**) The effect of drugs on the entry of plasmid DNA bearing a mCherry reporter. As in E, except

that cells were transfected with a mCherry-bearing plasmid. Error bars indicate SEM. N=dot

number. *, $p < 0.05$, *** $p < 0.001$ by unpaired Student t-test.

Figure 3 The effect of inhibitors on the actin cytoskeleton network.

(**A**) HEK293 ACE2-GFP cells were infected with SARS-CoV or SARS-CoV-2 PP in the

presence of Piceatannol as indicated. Luciferase expression was determined 48 h post infection

as an indicator of viral entry. Cells treated with the inhibitors without the virus were used to

determine drug toxicity. Error bars indicate SEM, N=4.

(**B**) Sunitinib partially protects Vero E6 cells from SARS-CoV-2-induced cytopathic effect

(CPE). Viability of Vero E6 cells was measured after treatment with the indicated drugs in the

presence (black curve) or absence (red curve) of the SARS-CoV-2 virus for 72 h. Error bars indicate SEM, N=2.

(**C**) Confocal images of U2OS cells stably expressing Tractin-EGFP, which have been treated with the indicated inhibitors at 10 µM (Mitoxantrone and Sunitinib 5µM) for 1h. Scale bar, 5 µm.

(**D**) TIRF images of drug-treated U2OS cells stably expressing Tractin-EGFP and mCherry-Clathrin light chain (CLC). CLC was used to focus on the plasma membrane. Scale bar, 5µm.

Figure 4 Mitoxantrone but not Banoxantrone binds heparin.

(**A**) The absorption spectra of Mitoxantrone (MTAN) and the structurally related chemical Banoxantrone (BTAN).

(**B**) Mitoxantrone binds heparin Sepharose. Mitoxantrone (50 µM) was incubated with either control Sepharose or heparin (HP)-coated Sepharose for 5 min. The picture shows the samples after centrifugation. The graph shows the absorbance spectra of the supernatant fractions.

(**C**) The interaction of heparin with Mitoxantrone changes its absorption spectrum. The absorption spectrum of Mitoxantrone (25 µM), heparin (25 µM), or Mitoxantrone+heparin (25 µM each) were determined by a NanoDrop spectrometer. The picture shows the color of the solutions.

(**D, E**) Banoxantrone (BANO) does not bind to heparin or HS. (D) Banoxantrone (50 µM) was incubated with heparin (HP)-coated Sepharose for 5 min. The picture shows the sample after centrifugation. The absorption spectrum of the HP-bead-depleted supernatant was measured together with a fraction of the input. (E) Banoxantrone (5 µM) was incubated with the indicated concentration of heparin or HS. A_{650} was measured. The changes in A_{650} after the addition of the oligosaccharides were plotted.

(F) The cytotoxicity profiles or Mitoxantrone and Banoxantrone in ACE2-GFP-expressing HEK293T cells. Error bars indicate SEM. N=3.

Figure 5 Gene expression analyses of Tilorone- and Mitoxantrone-treated cells.

(**A**) A heat map summary of the most induced or down-regulated genes by Tilorone treatment (T, 10 µM 6 h) or in untreated (U) HEK293T cells.

(**B**) A heat map summary of the most induced or down-regulated genes by Mitoxantrone treatment (M, 5 µM 6 h) or in untreated (U) HEK293T cells.

(**C**) A volcano plot shows the genes affected by Tilorone. Note that both the number of genes (shown by the number) and the scale of the expression changes in Tilorone-treated cells are small.

(**D**) A volcano plot shows the genes affected by Mitoxantrone.

(**E**, **F**) The CPE inhibitory activity and cytotoxicity of Tilorone and Raloxifene. Vero E6 cells were treated with Tilorone (E) or Raloxifene (F) in the presence (CPE) or absence of wild-type SARS-CoV-2. Cell viability was measured 72 h after treatment.

Supplementary movies

Movie 1

A U2OS cell expressing Tractin-EGFP.

Movie 2

The cell shown in movie 1 was imaged after treatment with Sunitinib 5 µM for 15 min. Note the increased assembly of actin filaments causes new filopodia formation on the cell surface.

Movie 3

A Tractin-EGFP-expressing U2OS cell was imaged after treatment with Sunitinib 5 µM for 60 min.

Movie 4

The same Tractin-EGFP-expressing U2OS cell in movie 3 was imaged at a different confocal plan where the stress fibers are located.

Movie 5

A U2OS cell expressing Tractin-EGFP.

Movie 6

The cell shown in movie 5 was imaged after treatment with BNTX 10 µM for 5min.

A
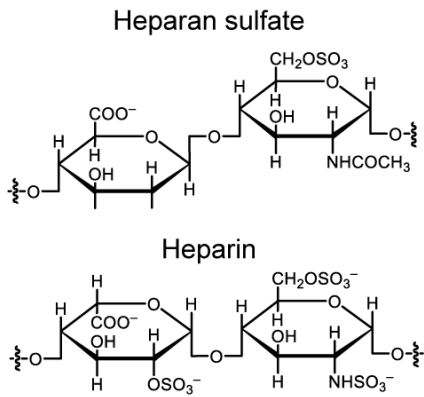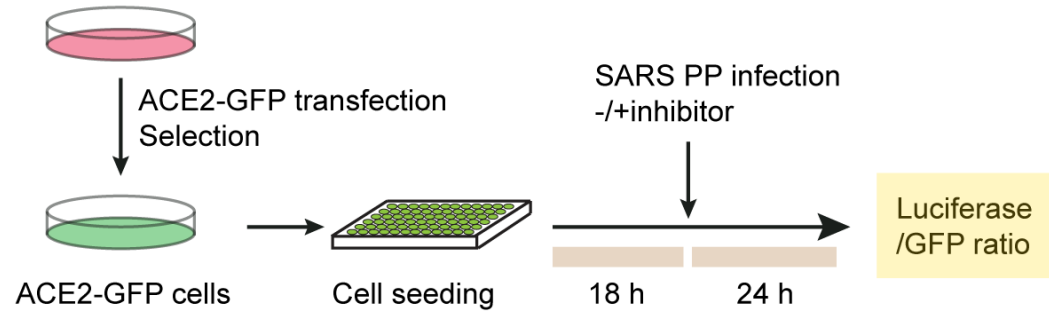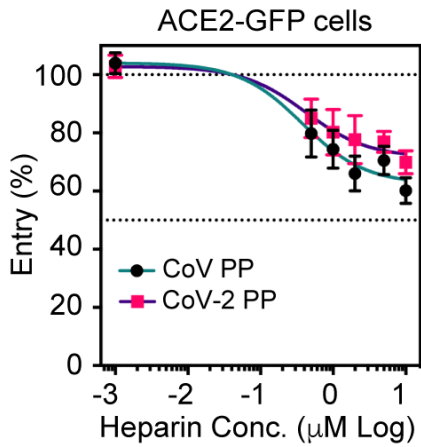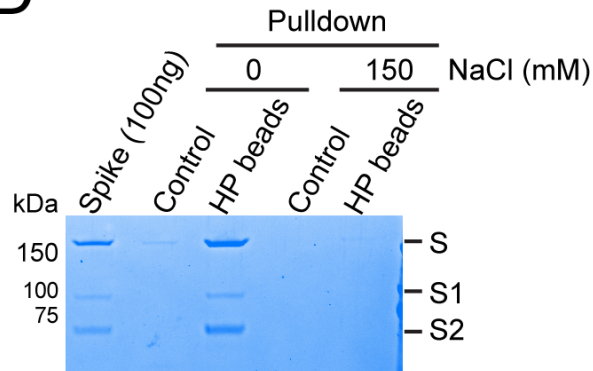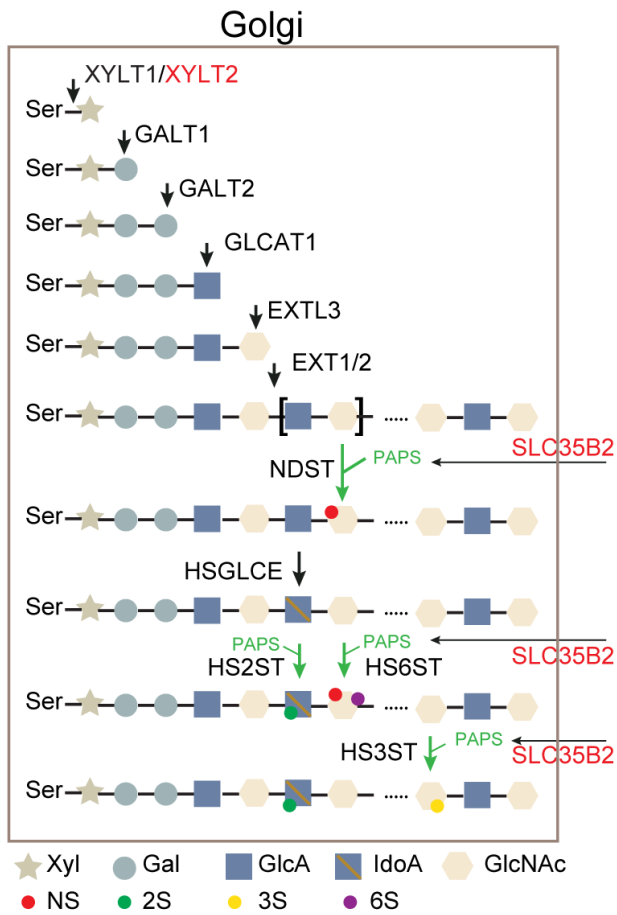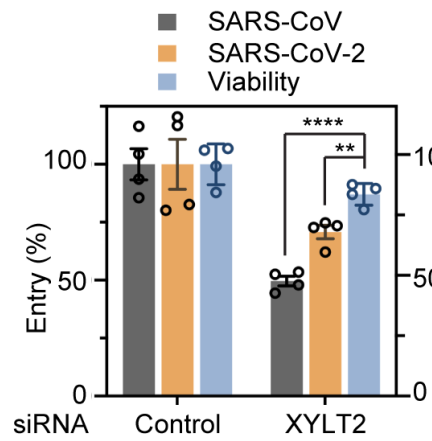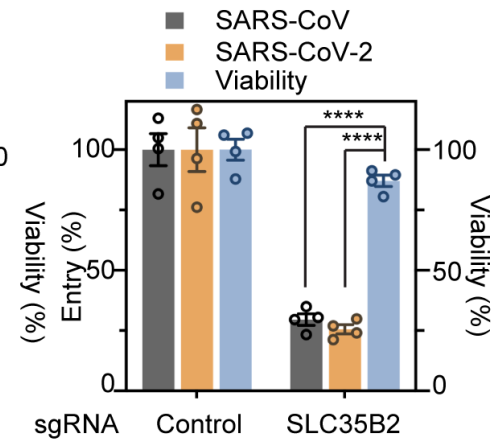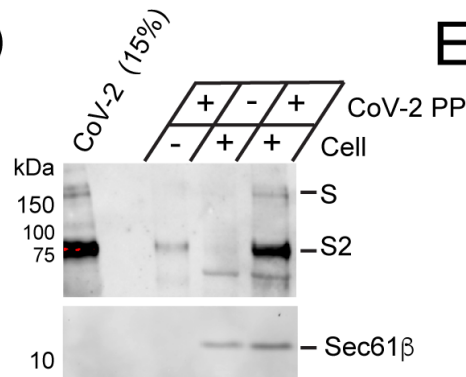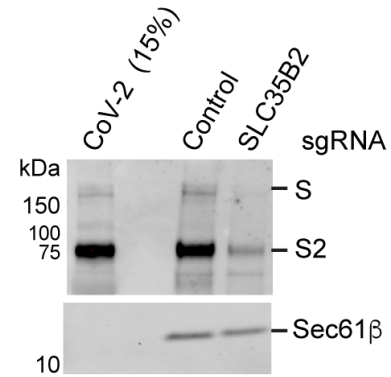
α-Syn fibril uptake assay
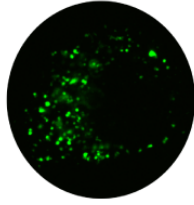
1280 drugs

Quantitative HTS

28

Manually sort-through

8

B

NO.	ID	*IC50 (µM)	DRUG INFO.
2#	NCGC00249050-02	4.4	Exifone, neuroprotective
6#	NCGC00095196-06	2.7	Tilorone, anti-virus
9#	NCGC00015693-09	0.08	Mitoxantrone, anti-cancer
10#	NCGC00015889-11	11.4	Raloxifene, hormone therapy against bone loss
12#	NCGC00164631-05	0.6	Sunitinib, RTK inhibitor anti-cancer
13#	NCGC00094226-07	10.2	BNTX, Opioid receptor antagonist
15#	NCGC00186034-01	6.5	K114, amyloid binding
16#	NCGC00024857-02	9.1	Piceatannol, anticancer and anti-inflammatory

C

Uptake inhibition   0%   100%

D

A

Mitoxantrone

B

C

P100

D

E

Mitoxantrone (MTAN)   Banoxantrone (BANO)

F

G

anti-Spike   ACE2-GFP
Spike